Atmospheric Environment 338 (2024) 120844

Contents lists available at ScienceDirect

Atmospheric Environment

journal homepage: www.elsevier.com/locate/atmosenv

Links between atmospheric aerosols and sea state in the Arctic Ocean

Alireza Moallemi [a,*,1], Alberto Alberello [b], Iris Thurnherr [c], Guangyu Li [c], Zamin A. Kanji [c], Filippo Bergamasco [d], Roman Pohorsky [a], Filippo Nelli [e,2], Alessandro Toffoli [e], Julia Schmale [a,**]

[a] Extreme Environments Research Laboratory, École Polytechnique Fédérale de Lausanne, Sion, Switzerland
[b] School of Mathematics, University of East Anglia, Norwich, United Kingdom
[c] Institute for Atmospheric and Climate Science, Department of Environmental Systems Science, ETH, Zurich, Switzerland
[d] Department of Environmental Sciences, Informatics and Statistics, Ca' Foscari University of Venice, Venice, Italy
[e] Department of Infrastructure Engineering, The University of Melbourne, Parkville, Australia

HIGHLIGHTS

- Sea surface state relation to coarse mode aerosol was studied over the Arctic Ocean.
- Aerosol concentration correlated stronger to sea state in unstable boundary layer.
- Wave height Reynolds number best parametrized the aerosol concentration variability.

GRAPHICAL ABSTRACT

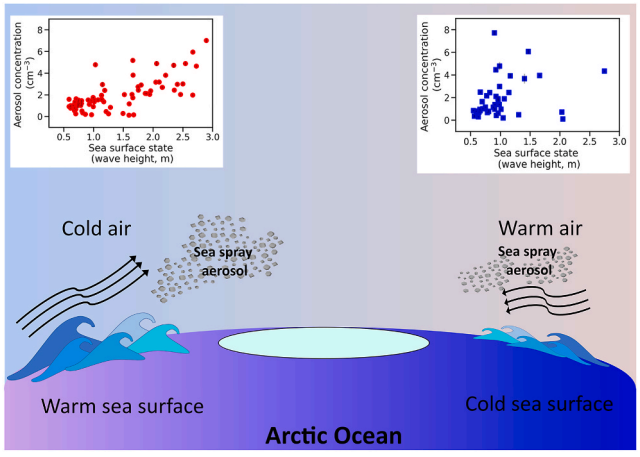

ARTICLE INFO

Keywords:
Sea spray aerosols
Wave height
Arctic ocean
Stereo imaging

ABSTRACT

Sea spray emission is the largest mass flux of aerosols to the atmosphere with important impact on atmospheric radiative transfer. However, large uncertainties still exit in constraining this mass flux and its climate forcing, in particular in the Arctic, where sea ice and relatively low wind speed in summer constitute a significantly different regime compared to the global ocean. Sea state conditions and marine boundary layer stability are also critical variables, but their contribution is often overlooked. Here we present concurrent observations of sea state using a novel stereo camera system, of sea spray through coarse mode aerosols, and of meteorological variables to determine boundary layer stability in the Barents and Kara Seas during the 2021 Arctic Century Expedition. Our findings reveal that aerosol concentrations were highest over open waters, closely correlating with wave height,

* Corresponding author.
** Corresponding author.
E-mail addresses: alireza.moallemi@nrc-cnrc.gc.ca (A. Moallemi), julia.schmale@epfl.ch (J. Schmale).
[1] Now at: Metrology Research Centre, National Research Council of Canada, Ottawa, Ontario, Canada.
[2] Now at: Department of Mechanical Engineering, Swinburne University of Technology, Hawthorn, Australia.

https://doi.org/10.1016/j.atmosenv.2024.120844
Received 8 May 2024; Received in revised form 18 September 2024; Accepted 25 September 2024
Available online 26 September 2024

followed by wind speed, wave steepness, and wave age. Notably, these correlations were stronger under unstable marine boundary layer conditions, reflecting immediate sea spray generation. By analysing various combinations of sea and atmospheric variables, we identified the wave height Reynolds number as the most effective indicator of atmospheric sea spray concentration, explaining 57% of its variability in unstable conditions. Our study underscores the need to consider sea state, wind, and boundary layer conditions together to accurately estimate atmospheric sea spray concentrations in the Arctic.

1. Introduction

Oceans cover about 70% of Earth's surface and are a vital component of the climate system (Rogers, 1995). The interaction between the oceans and atmosphere involves a perpetual exchange of energy, mass, and momentum, which derive the emissions of sea spray aerosol (SSA) particles (Andreas, 1992; Lewis and Schwartz, 2004) through wave breaking processes (Veron, 2015). These particles vary widely in size, ranging from tens of nanometres to hundreds of microns, existing in both liquid and solid phases (Lewis and Schwartz, 2004; Veron, 2015). Depending on their size, SSA can reside in the atmosphere for seconds to days before removal through dry or wet deposition pathways (Veron, 2015). While in the atmosphere, SSA exert a radiative forcing by scattering and absorbing solar radiation (Claeys et al., 2017; Lundgren et al., 2013), influencing the atmospheric energy budget. SSA are excellent cloud condensation nuclei and hence also impact atmospheric radiative transfer through cloud formation and influencing cloud properties such as albedo and lifetime (Andreae and Rosenfeld, 2008; DeMott et al., 2016; Fitzgerald, 1991; Mason, 2001; Xu et al., 2022). In the Arctic, SSA is a dominant component of the aerosol population (e.g., Moschos et al., 2022).

The Arctic has been warming at an accelerated rate compared to other regions (Manabe and Wetherald, 1975; Meredith et al., 2019). Clouds have been contributing significantly to polar amplification. While they exert both cooling and warming effects through the scattering of shortwave radiation and absorption of longwave radiation, respectively (Alkama et al., 2020), there is evidence that clouds produce a net warming effect over the Arctic pack ice (Shupe and Intrieri, 2004). As Arctic amplification progresses and sea ice continues to retreat, larger areas of the Arctic Ocean are becoming exposed to the atmosphere (Cabral et al., 2022), enhancing SSA production (Struthers et al., 2013) and increasing cloud formation with a yet largely unconstrained cloud radiative effect, which predominantly cools over the open ocean (Middlemas et al., 2020).

Existing climate models show notable uncertainties relative to SSA parametrizations. Lapere et al. (2023) examined 12 climate models and revealed a fivefold variation in the estimation of SSA surface mass concentration across different models. Furthermore, Lapere et al. (2023) identified substantial biases up to one order of magnitude, when comparing the models' SSA estimations with observational data from ground stations. This is attributed to uncertainties in the SSA source functions, which govern the emission of SSA fluxes into the atmosphere. The process is regulated by the breaking of wind-driven surface waves, which entrains air into the water, generating bubbles that rise to the sea surface and burst (Monahan et al., 1986). If wind forcing is strong, SSA originate from spume droplets which are torn out from the ocean surface and propelled into the atmosphere directly (Lewis and Schwartz, 2004).

Parameterization of SSA source terms in numerical models are generally uncertain, with difference across various parameterizations exceeding one order of magnitude (de Leeuw et al., 2011). This is attributed to the oversimplification of SSA flux functions, which mainly rely on wind forcing and, thus, neglecting air-fluid dynamics at the sea surface (Hristov et al., 2003). Recognizing this limitation, recent efforts have focused on incorporating wave properties (height, steepness and age) and other sea state related properties (white cap coverage and surface temperature) (Bruch et al., 2021; Demoisson et al., 2013; Lafon et al., 2007; Laussac et al., 2018; Lenain and Melville, 2017; Monahan and O'Muircheartaigh, 1986; Norris et al., 2013; Ovadnevaite et al., 2014). Some of these approaches used dimensionless parameters, such as the Reynolds number, to jointly consider atmospheric and sea state variables in their parameterizations (e.g., Bruch et al., 2021; Lenain and Melville, 2017). Nevertheless, field studies with collocated sea state and atmospheric aerosol measurements are scarce, and there is a need for larger datasets to both validate existing models and develop more accurate and reliable parameterizations, in particular in the Arctic, where sea state can be influenced by sea ice and stably stratified boundary layer conditions.

The challenge in compiling extensive datasets of concurrent atmospheric and oceanic variables resides with sea state measurements. In situ techniques such as buoys have been extensively used (Ardhuin et al., 2019; Rossi et al., 2022). However, the operation and maintenance of in situ instruments are both costly and time-consuming. On the other hand, ocean surface properties can be characterized by various remote sensing methods, including laser altimeters (Xu et al., 2021), light detection and ranging (LiDAR) systems (Irish et al., 2006), and radar systems (Dankert et al., 2003; Derkani et al., 2021). However, these methods are either expensive or face challenges in field deployment, posing obstacles for extensive datasets. A promising technique is stereo imaging (Schumacher, 1939). Over the past 20 years, with the advent of digital imaging technologies and enhanced computational power, this application has become much more accessible. Relative to ocean waves, applications have been proposed from both fixed and moving marine platforms (Alberello et al., 2022; Benetazzo, 2006; Benetazzo et al., 2015; Malila et al., 2022; Schwendeman and Thomson, 2017; Smith and Thomson, 2020; Toffoli et al., 2023; Waseda et al., 2022). As sensors are becoming more accessible, and data analysis toolkits more sophisticated and computationally affordable (e.g., Bergamasco et al., 2017), stereo imagery provides a cost-effective solution. Furthermore, the capability to operate aboard moving platforms (i.e., ships), make them ideal to integrate wave measurements with SSA observation (Schmale et al., 2019).

Here we discuss an application of stereo imagery with concurrent measurements of the atmospheric boundary layer and aerosols to study the interaction of wind, waves, and atmospheric characteristics with aerosol occurrence. Instruments were deployed on the research vessel *Akademik Tryoshnikov,* which operated across the Arctic Ocean throughout the summer of 2021 (the Arctic Century Expedition). Details of this expeditions are reported in Section 2 together with the methodology employed for data collection and processing. In Section 3, we present the characteristics of atmospheric and sea surface measurements, and assess which combination of wave and wind properties explain the variability of aerosol number concentration. Concluding remarks are presented in section 4.

2. Methodology

2.1. Arctic Century Expedition

The Arctic Century expedition took place aboard the research vessel *Akademik Tryoshnikov* from August 5 to September 6, 2021, in the Russian sector of the Arctic Ocean. The expedition started at Murmansk in Russia, and covered vast regions of the Arctic, north of the Taymyr peninsula, including, Franz Josef Land, Severnaya Zemlya, and Kara Sea, before returning to Murmansk (details of the route are reported in

Fig. 1). For this study, we focus on the Kara Sea region, where data were recorded (see colored points in Fig. 1). During the voyage collocated data of sea state parameters, atmospheric characteristics, and aerosol properties were gathered underway.

2.2. Sea state observation: stereo imaging set-up

We collected stereo images of the sea surface through an image acquisition system consisting of two synchronised GigE monochrome industrial CMOS cameras equipped with 5 mm lenses to produce a field of views of ~90°. The equipment was mounted on the guardrails of the second deck of the ship at approximately 11.5 m above sea level facing the starboard side of the ship. The distance between the two cameras (baseline) was 3 m and they were tilted downwards ~ 20°, i.e. towards the sea surface plane. Sequences of images were acquired during a period of 20 min every hour at a sampling rate of 2 Hz. The cameras were calibrated at the end of the voyage to retrieve intrinsic parameters needed for the image processing.

2.3. Sea surface data processing

We use the open-source software Wave Acquisition Stereo System (WASS, Bergamasco et al., 2017) to reconstruct the sea surface in 3D from stereo image sequence data. WASS processes the individual stereo frames within a given sequence and identifies the pixel-to-pixel correspondence from one camera image to the other (correspondence points). Given that the relative position and orientation between the cameras is known, the WASS stereo algorithms reconstruct a 3D point clouds of the sea surface. It should be noted that as part of the process WASS automatically estimates the relative position and orientation of one camera compared to the other and integrates that information when conducting the 3D reconstruction. Furthermore, for each stereo frame within a sequence, WASS automatically filters outliers and, by fitting a plane through the point clouds, estimates the mean sea plane relative to the cameras. Details of different algorithms used in WASS are thoroughly explained in Bergamasco et al. (2017). It should be noted that the position of the cameras relative to the sea surface can change due to the motion of the ship. Based on the analysis of a subsample of sequences, we verified that the relatively calm sea states that occurred during Arctic Century produce only a small impact on the reconstructed wave parameters. On average the uncertainties in wave height are as low as 10 cm. Therefore, corrections for ship motion were omitted (a similar approach was used in Waseda et al., 2022). We linearly interpolated the point cloud data within a 30 m × 30 m square area (assuming a grid resolution of 0.03 m) located 45–70 m away from the imaging system. Fig. 2 summarizes the WASS processing workflow of extracting point clouds from stereo images.

It should be noted that the success of the WASS algorithm to identify correspondence points and carry out the 3D reconstruction highly depends on the sea surface scene captured by the imaging system. For instance, in our dataset strong sun glint significantly reduced the number of reconstructed point clouds or even prevented WASS from successfully running its process for several stereo frames within given sequences. Thus, the reconstructed sea surface was not always homogeneously distributed within the field of view and gaps within a sequence of reconstructed data were common. In our analysis we considered therefore only samples that contained at least 5 min of point cloud data with sequential gaps smaller than 3.5 s.

Time series of the surface elevation $\eta(t)$ were extracted at 5 different points within the interpolated area of the sea surface. Fig. 2b shows the relative location of the extracted points compared to the interpolation area and Fig. 2c shows an example of $\eta(t)$. For the signal processing we initially filled the gaps in $\eta(t)$ using a polynomial interpolation of 2nd order. $\eta(t)$ was used to compute the wave energy spectrum. The latter was then used to infer basic parameters including:

the significant wave height H_0

$$H_0 = 4\sqrt{m_0} \tag{1}$$

where m_0 is the zeroth order moment of the wave spectrum and was extracted by WASS;

the mean energy period, τ, as

$$\tau = \frac{\int f^{-1} S(f) df}{\int S(f) df} \tag{2}$$

where f is the frequency and $S(f)$ is the spectral energy, both as extracted by WASS, noting that among many forms of the wave period this is the more stable;

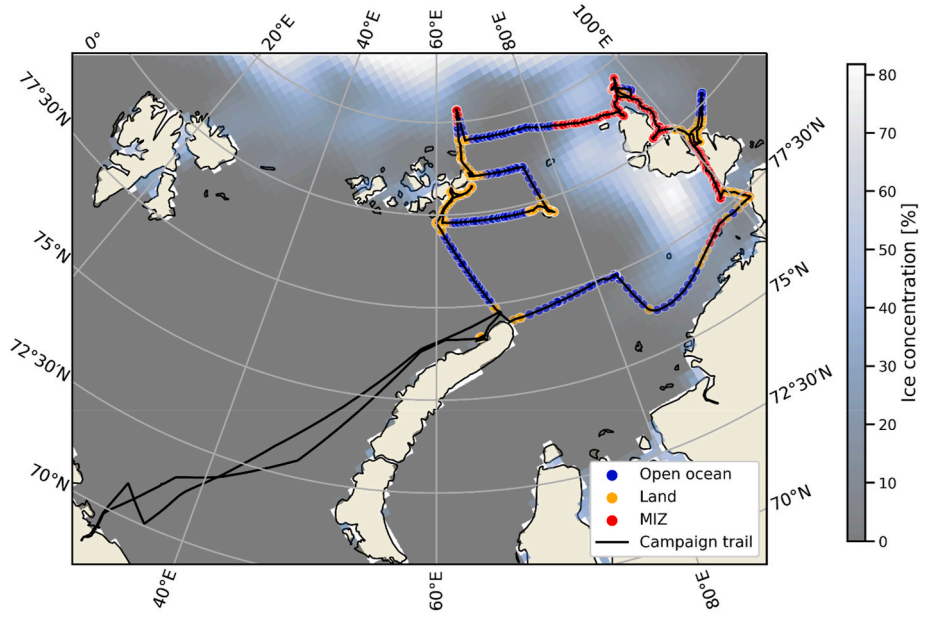

Fig. 1. Track of the Arctic Century 2021 Expedition map. Different colored markers correspond to where data was recorded and the different specified geographical zones. The displayed ice cover data corresponds to the average ice concentration during the campaign period (AMSR-2, Copernicus Climate Change Service (C3S), 2020).

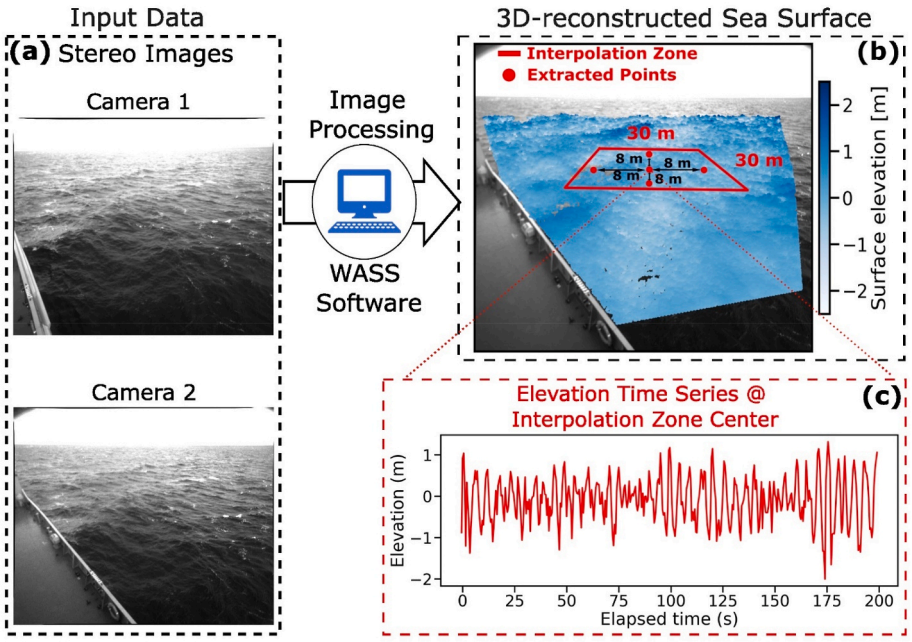

Fig. 2. The workflow of processes involved in extraction of sea surface elevation time series, $\eta(t)$, from of stereo images. (a) is an example of stereo images taken on 2021-08-18. (b) shows the reconstructed sea surface after processing the stereo images through WASS. The red line is the interpolation area (with its dimensions) and the red dots are the points where we extracted the sea surface elevation time series in our analysis. (c) shows an example of a portion of $\eta(t)$ at the centre of the interpolation zone.

the wave speed, c,

$$c = g\frac{\tau}{2\pi} \tag{3}$$

and the wave steepness, ε,

$$\varepsilon = H_0 \times \frac{2\pi^2}{g\tau^2} \tag{3}$$

The Doppler effect induced by the ship's forward speed which influences τ was removed (see Alberello et al. (2022) for details). By combing the aforementioned basic wave properties with wind speed, data is used to construct additional pertinent parameters, including:

The wave-height-based Reynolds number, Re_H,

$$Re_H = \frac{H_0 \times U_{10N}}{\nu_w} \tag{6}$$

where U_{10N} is the neutral wind speed at height of 10 m and ν_w is the sea water kinematic viscosity;

and the wave age, WA,

$$WA = \frac{c}{U_{10N}}$$

Bruch et al. (2021) suggested that it is physically more meaningful to use the inverse of WA (WA^{-1}) when studying the relation between sea surface properties and SSA, as WA^{-1} is expected to co-vary positively with other properties, such as *Re*. In our analysis we adapted a similar approach to Bruch et al. (2021) and used WA^{-1}, when assessing possible correlations between aerosol particles and wave properties

2.4. Atmospheric measurements

2.4.1. Meteorological and sea water data'

A weather station (model AWS420, Vaisala) installed on *Akademik Tryoshnikov* provided measurements of ambient temperature and relative humidity at 23.7 m above sea level (ASL), ambient pressure at 20 m ASL, and wind speed and horizontal direction at 30.5 m ASL (at the starboard side). An additional anemometer (Model WXT532, Vaisala) provided wind speed and direction on the port side at 30.5 m ASL. The measurements from the weather station were processed by the Vaisala acquisition software providing the true and relative wind speeds and directions at a temporal resolution of 0.33 Hz. It is known that the ship structure influences the surrounding fluid flow and promotes turbulence resulting in occasional inconsistencies between the measurements from the two wind sensors (Landwehr et al., 2020). Based on the comparison of the wind direction and speed measurements from the two sensors with data from the European Centre for Medium-Range Weather Forecasts fifth generation atmospheric reanalysis of the global climate (ERA5), Landwehr et al. (2020) estimated the wind flow distortion effect of *Akademik Tryoshnikov* allowing for the correction of the raw wind speed data. In this study we used the Landwehr et al. (2020) methodology to correct for the flow-distortion effect on the wind speed measurements. While the corrected wind speed measurements (U) correspond to a height of 30.5 m ASL, the scientific community conventionally employs the neutral wind speed at ASL of 10 m (U_{10N}). Landwehr et al. (2020) estimated U_{10N} from U measurements by using ship-track interpolated surface heat flux data from ERA5 and the COARE 3.5 bulk flux model. In our analysis we used the Landwehr et al. (2020) method to convert U measurements to U_{10N} using ERA5 data for the campaign duration (Hersbach et al., 2023).

In addition to observed atmospheric properties, the stability of the atmospheric boundary layer (BL) was estimated as the difference between atmospheric temperature (T_{atm}) and sea surface temperature (*SST*). In absence of continuous sea surface temperature measurements, we used the SST reanalysis data from ERA5 (Hersbach et al., 2023) which were spatially interpolated to the ship location and for a few periods near land masses where SST data were not available, we applied a temporal interpolation to the *SST* data. Mixing field observations and re-analysis data is an unconventional approach. However, we note that SST from ERA5 is generally accurate and matches well against field observations (see Tersigni et al., 2023).

2.4.2. Aerosol measurements

Ambient aerosol measurements were conducted by a suite of online aerosol instruments combined with off-line sample collection in a

container located in deck 2 of the ship at an elevation of ~11 m above sea surface level (for more detailed information see Schmale et al. (2019), where a near-identical set-up was used). Ambient air was sampled through a custom-built inlet with a vertical length of 4.5 m while maintaining a maximum sample temperature of 40 °C. Inside the container a flow splitter was employed to distribute the ambient samples to online instruments and an offline sampler. Sample lines were distributed isokinetically to online instruments with sample flow rates ranging from 0.283 L min^{-1} to 1 L min^{-1}. While various microphysical properties of aerosols were measured, here we primarily focus on particle number size distribution (PNSD) measurements and aerosol chemical composition. More details regarding the aerosol sampling container can be found in Li et al. (2022, 2023).

Offline aerosol samples were collected by an impinger (Coriolis® μ, Bertin Instruments, France) which has a steady sample flow rate of 300 L min^{-1}. The impinger sample period was 3 h and 75 samples were collected through the campaign. Chemical composition of aerosol samples collected by the impinger were analysed using inductively coupled plasma-optical emission spectrometry (ICP-OES, Model 5100, Agilent Technologies) to detect the abundance of 11 elements (Al, Ca, Cl, Fe, K, Mg, Mn, Na, P, S, Si). To assess the measurement quality, standard reference material and blank samples were measured (more details on the chemical analysis can be found in Gilli et al. (2018). In this study, we considered the sum of Al, Si, and Ca concentrations to be dust indicators while the sum of Na and Mg concentration are considered as sea salt indicators after Hiranuma et al. (2013).

Coarse-mode PNSD was measured by an aerodynamic particle sizer (APS, model 3321, TSI Inc.), with a temporal resolution of 4 min. The APS provided the size resolved aerosol number concentration in 52 logarithmically equi-spaced size bins between 0.5 and 20 μm. In this study we confined our analysis to the coarse aerosol size range above the aerodynamic diameter of 0.7 μm for two main reasons. Firstly, since in a remote Arctic marine environment in summer the prevalence of SSA compared to other atmospheric aerosol species is expected to be larger in the coarse size range (Song et al., 2021), allowing us to draw conclusions on SSA wave interactions directly from measurements. Secondly, the lower 0.7 μm threshold for analysis of APS data was suggested by Schmale et al. (2019), as they observed an overestimation in number concentration measurement by the APS for size bins below 0.7 μm for atmospheric aerosol data. Throughout this work, we refer to the aerosol number concentration measured by APS with aerodynamic diameters larger than 0.7 μm as $N_{0.7}$.

An intrinsic limitation of ship-borne aerosol sampling is the occasional sample contamination by the exhaust emission from the ship stack. Such contaminations could create biases in the data that may complicate data interpretation. We use the Beck et al. (2022) methodology to identify and remove the sample periods contaminated by ship exhaust. In this method the temporal variability in an aerosol particle counter (e.g., APS measurement) is used to construct a pollution flag which identifies the contaminated periods of aerosol samples. In our analysis we used the APS total particle number concentration measurements and applied the interquartile range (IQR), median, and sparse filters. The IQR factor was set to 1.7 with IQR window of 1440 min, and an upper threshold of 300 cm^{-3} with the neighbour decision activated. The median time window was set to 30 min and the median factor was 1.5. The sparse filter had a window of 30 data points and a threshold of 20 data points. Applying the pollution filter to APS data resulted in approximately 22% of the data points being identified as polluted samples and they were discarded.

2.5. Geographical division of the dataset

During the Arctic Century Expedition, on numerous occasions the research vessel approached land masses (e.g., Franz Josef Land and Severny Island) and traversed through regions where the sea surface was partially covered with ice. Studies have shown that proximity to land masses and presence of sea ice can impact the concentration of sea spray aerosol and their production mechanism (e.g., Moallemi et al., 2021).

Thus, when assessing the links between sea surface state and SSA production it is important to account for the specific geography of the campaign region. The sea state mainly depends on the wind fetch (i.e., the unobstructed length that the wind can traverse over the open ocean) which is highly influenced by the proximity to land masses. In our analysis, we define data points closer than 50 km from land as "land", and further away than 50 km as ocean, i.e., the fetch is unaffected by land masses. Another factor that can impact the production of sea spray aerosol especially in the polar regions, is the interaction of waves with sea ice. For example, Yan et al. (2020) showed that the sea spray aerosol number concentration in the marginal sea ice zone is greater than over the open ocean regions in the Southern Ocean. Thus, to distinguish different possible mechanisms of SSA production on the basis of the geography, we divided the dataset into three different zones (see color code in Fig. 1): *open ocean* (samples acquired further than 50 km from land masses), *land* (samples acquired closer than 50 km from land masses), *marginal ice zone* (MIZ) defined as the area where the sea ice coverage was between 15 % and 80 % (Rolph et al., 2020; Strong and Rigor, 2013). The sea ice concentration was obtained from AMSR-2 daily satellite measurements (Copernicus Climate Change Service (C3S), 2020) and interpolated to the ship coordinates.

3. Results

3.1. Aerosol measurements and source assessment

As a first step to investigate the possible sources of aerosols, we calculated the count median diameter (CMD) from the aerosol size distribution measurements. The kernel density distribution of the CMD (Fig. S1) is bimodal with a distinct minimum at ~0.99 μm, suggesting the existence of two possible populations of aerosol samples, namely a "coarse group", N_c (CMD >0.99 μm), and "fine group", N_f (CMD ≤0.99 μm). The normalized aerosol number size distributions of N_f and N_c are different (Fig. 3), and, while both cases demonstrate a monotonic decrease in number concentration as size increases, the size resolved concentration of N_f (Fig. 3a) decreases much more steeply than N_c (Fig. 3b). The size distribution results indicate that the relative contribution of aerosols within the size range of 1–3 μm is noticeably larger for N_c compared to N_f cases. Note that both populations span the entire size range measured by the APS but have distinct CMDs. The large contribution of the 1–3 μm aerosol to the size distribution is expected for primary aerosol, such as SSA and dust (Hess et al., 1998). The offline aerosol chemical composition data provide further information on the possible origin of the aerosol particles. Following the standards introduced in Hiranuma et al. (2013), we considered the combined aerosol mass concentration of Na and Mg (Na + Mg) as a proxy for SSA and the combined aerosol mass concentration of Al, Si, and Ca (Al + Si + Ca) as a proxy for dust aerosols. The volume concentration of the coarse group sample was strongly correlated to Na + Mg (Fig. S2) with the Pearson correlation coefficients (r_p) of 0.9 supporting the possibility of N_c association with SSA. On the other hand, the correlation of coarse aerosol volume concentration to Al + Si + Ca was noticeably lower ($r_p = 0.63$) compared to Na + Mg. Together with the fact that much higher concentrations of Na + Mg than Al + Si + Ca occurred, we interpret these observations as an indication that N_c aerosols are more likely associated with sea salt than other particle types. It should be noted that Ca can also be present in SSA (Mukherjee et al., 2020), but it is difficult to disentangle the contribution of Ca from either dust or SSA. The fine aerosol shows weak correlation with Na + Mg ($r_p = 0.36$) and Al + Si + Ca ($r_p = -0.17$). The low correlation may suggest that N_f are less likely associated with either dust or SSA mass concentrations, but the results must not be overinterpreted since the total number of data points for the fine aerosol samples for which chemical composition is available is relatively low (see Fig. S2). As the N_c observations demonstrated characteristics

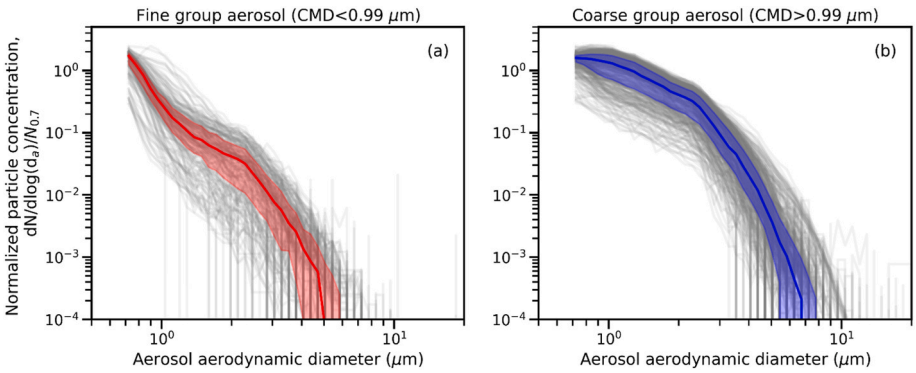

Fig. 3. The aerosol particle size distributions normalized by the total number concentration. (a) fine aerosol class N_f and (b) coarse aerosol class N_c. The grey lines are the individual observations and the solid red and blue lines corresponds to the median values bounded by the inter quartile range in colored shared areas (IQR).

that are aligned with expected SSA properties, hereafter in our analysis we mainly focus on N_c when discussing aerosol results. We denote the number concentration of coarse group aerosols as $N_{0.7c}$.

The time series of the hourly averaged integrated aerosol number concentration, $N_{0.7}$, is shown in Fig. 4a, (with indications for N_f and N_c contributions). The median $N_{0.7}$ over the whole campaign was 0.52 cm^{-3} with and interquartile range (IQR) of 0.24–1.2 cm^{-3} and a maximum of 7.7 cm^{-3}. The average aerosol volume concentration was 1.8 ± 2.6 $\mu m^3/cm^3$ (mean ± standard deviation) which is within a similar range of the values reported in the literature for the Barents Sea, Kara Sea and Greenland Sea in Summer of 2021 for aerosols with optical diameter larger than 0.5 μm (1.42 ± 3.09 $\mu m^3/cm^3$(Sakerin et al., 2022);). The time series of aerosol measurements indicates that the baseline concentration of $N_{0.7}$ is interrupted by multiple high aerosol concentration events characterized by occasional peaks in the $N_{0.7}$ time series (Fig. 4a). High concentration events with peaks above 2 cm^{-3} consist mainly of N_c samples suggesting that these events are likely driven by larger atmospheric aerosols, i.e., SSA (and less likely dust).

3.2. Regional variability of meteorological, wave and aerosol properties

During the campaign, U_{10N} varied within an order of magnitude ranging from 0.3 to 11.3 m/s with a median value of 4.7 m/s (Fig. 4b). The upper range for the observed wind speed is smaller than the anticipated wind speed for the Barents Sea and Kara Sea regions which are expected to be around ~20–25 m/s for August and September based on a trend analysis study based on ERA5 reanalysis data (Cabral et al., 2022). Despite low wind speed, the median U_{10N} (4.7 m/s) is above the threshold of 4 m/s, the onset of sea spray production (Monahan and O'Muircheartaigh, 1986). Hence, it is expected that wind speed

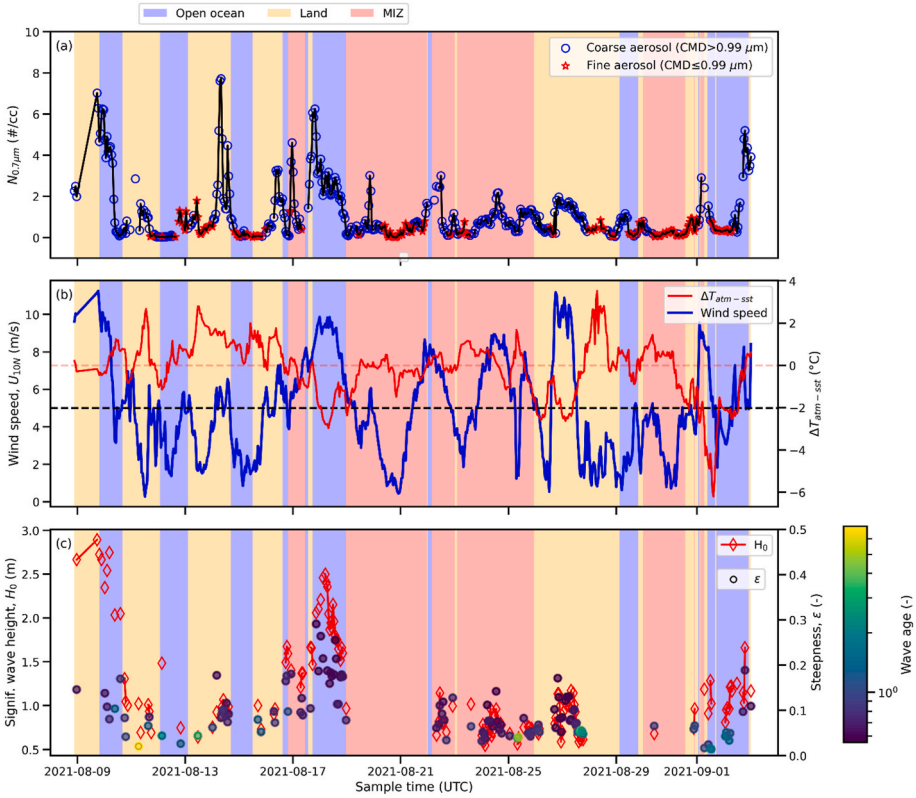

Fig. 4. Time series of (a) aerosol number concentration ($N_{0.7}$), (b) neutral wind speed at 10 m above sea level, U_{10N}, and difference between atmospheric temperature (T_{atm}) and SST ($\Delta T_{atm\text{-}SST} = T_{atm}$ - SST), and (c) H_0 and ε (color-coded by wave age). The colored background refers to areas of open ocean (blue), "land" (yellow) and within the MIZ (pink).

variability influenced $N_{0.7c}$. The atmospheric stability (Fig. 4b) is a proxy for the turbulence in the marine boundary layer (MBL) and thus impacts the dispersion of SSA. It can be characterized by the difference in atmosphere and sea surface temperatures ($\Delta T_{\text{atm-sst}}$) with $\Delta T_{\text{atm-sst}} > 0$ °C corresponding to a stable MBL and $\Delta T_{\text{atm-sst}} < 0$ °C representing an unstable MBL condition (Lewis and Schwartz, 2004; Tedeschi and Piazzola, 2011). The median value of $\Delta T_{\text{atm-SST}}$ was −0.02 °C with an IQR of −0.92 °C to 0.67 suggesting that the MBL is skewed towards unstable conditions (Fig. 3b), i.e., warmer SST than air that enhances turbulence and, hence, capacity for particle take off and atmospheric transport.

Wave height and steepness (Fig. 4c) generally co-vary with wind speed but their magnitudes are dampened in the vicinity of the MIZ and land (colored background of Fig. 4). The wave age is independent of the ship location and more than 50 % of the data points correspond to an age >1, where the wind cannot induce wave breaking. Due to the sun-glint and fog interferences, the contamination of the camera windows by droplets, ice-packed sea surface, and calm featureless sea surface images, the number of sample points for which the stereo system was applied successfully is limited (141 points) and that is why measurement gaps exist in certain periods. For the investigated period, the median value of H_0 was 0.99 m with an IQR of 0.75 m–1.48 m and minimum and maximum values of 0.55 and 2.9 m, respectively. The average and range of H_0 values are consistent with wave heights estimates reported for the Kara Sea region in the literature. For instance, based on altimeter data and hindsight models, Stopa et al. (2016) estimated a value of ~1.2 m for the average wave height in the Kara Sea for the month of August. Duan et al. (2019) estimated the range of significant wave height to be 0.5–2.5 m for the northern zone of the Kara Sea and 0.5–2 m for the southern zone. The τ (not shown in Figures) has a median value of 4.9 s with an IQR of 4.5–5.5 s and minimum and maximum values of 3.2 and 12.7 s, respectively. Duan et al. (2019) estimated the range of wave periods to be 4–7 s and 3–6 s in the northern and southern zones of the Kara Sea, respectively, which is consistent with the range of variability observed in our study for τ.

Fig. 5a, shows the range of variability of U_{10N}, SST, MBL stability, H_0, ε, wave age, aerosol diameter and number concentration for the different regional sectors (ocean, MIZ and land). The median values of U_{10N} are similar across the different sectors, changing between 4.9 m/s (in the open ocean sector) to 4.5 m/s (in the land sector). Conversely, the inter quartile ranges (IQR) of U_{10N} demonstrate more notable difference between regions, where the IQR over the open ocean is ~1.5 times larger than over the other sectors, likely due to the larger number of data points.

Previous studies have shown the significance of *SST* on SSA production (e.g., Jiang et al., 2021; Song et al., 2023; Zinke et al., 2022). In our dataset, *SST* values (from ERA5 reanalysis, Fig. 5b) were constrained within the −1.8° to 5 °C range, thus our sample is representative of conditions just above the sea ice freezing point. The *SST* in the open ocean region was systematically higher than in the other regions. The

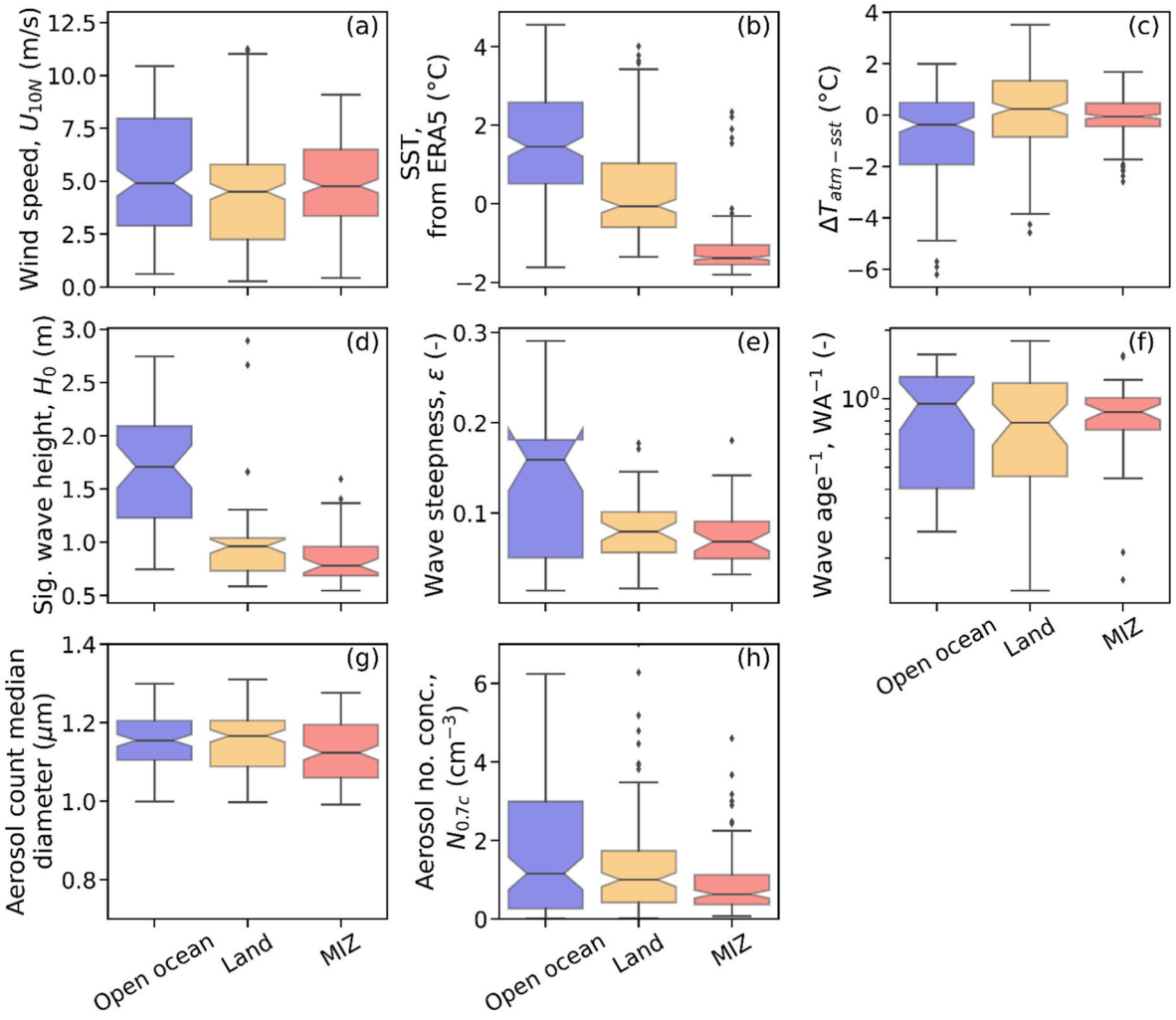

Fig. 5. Boxplots of different aerosol, wave, and environmental measurements in the three specified regions of open ocean (samples acquired further than 50 km from land masses), land-influenced (samples acquired closer than 50 km from land masses) and marginal ice zone (MIZ, where ice concertation is between 15 and 80%).

open ocean median *SST* (1.5 °C) was 1.6 °C and 2.9 °C larger than the median *SST* on the land and MIZ regions, respectively. Generally, we suspect that due to the narrow range of variability in *SST*, its impact of modulating SSA production in our dataset is however minimal.

The *SST* over open ocean was typically warmer than the air thereby inducing an unstable MBL that enhances turbulence and, hence, capacity for particles to be dispersed vertically and participate in atmospheric transport. This condition is more evident over the open ocean and MIZ than over land (Fig. 5c), noting that the MIZ distribution is overall close to 0 °C due to the presence of sea ice.

For H_0 (Fig. 5d), the largest median value (1.7 m) and IQR (1.2–2.1 m) was observed in the open ocean region, while the smallest median (0.8 m) and IQR (0.7–1 m) was observed in the MIZ. For the land region, the median H_0 was 1 m and the IQR was similar to the MIZ. Similarly, to H_0, for ε (Fig. 5e), the largest median (0.16) and IQR (0.05–0.18) occurred in the open ocean. The median (and IQR) ε for the land and MIZ regions were 0.08 (0.06–0.1) and 0.07 (0.05–0.09), respectively. Wave age (Fig. 5f), is generally younger over the open ocean compared to the MIZ and land regions. The wave properties appear to be quite similar among the land and MIZ regions, while in contrast the median and IQR in the open ocean region are ~2 and 3 times larger than the values in the other regions. The significant differences between the wave properties over open ocean and other regions suggest that the sea surface state was much calmer near land masses and in the MIZ during the campaign, which is expected due to the attenuation of waves by sea ice and the lower fetch near land masses which can limit the wave development. The median value of the wave age is quite similar between the different regions ranging from 1.1 in the open ocean to 1.3 in the land region suggesting that in most cases the wind and wave speeds are within the same range. However, the range of variability of wave age for MIZ samples appears to be much smaller than the other regions, which, is attributed to the attenuation of high frequency wind-driven waves once they interact with ice floes in the MIZ (Alberello et al., 2022), which limits the wave speed variability and thus the wave age.

Considering all six variables together (Fig. 5a–f) it becomes evident that over the open ocean, more wave breaking likely occurred due to stronger wind, steeper and younger waves, and that conditions for dispersion of SSA were favourable due to the MBL instability. Fig. S3 shows 4 examples sea surface images taken over open ocean regions for which the H_0 values were above 2 m.

Fig. 5g and h shows the regional variability in the $N_{0.7c}$ *CMD* and $N_{0.7c}$ number concentration. Generally, the open ocean and land regions have similar aerosol properties while the MIZ has slightly smaller *CMD* and systematically smaller $N_{0.7c}$ compared to the other regions. The results indicate that the MIZ has the lowest SSA production relative to the other regions for the particle size range considered here. Our results challenge the findings by Yan et al. (2020) who, based on a dataset collected over the Southern Ocean, suggested the solid-fluid interaction in the MIZ enhances the production of primary marine aerosols compared to the open ocean environments. The climate and meteorological differences between the investigated regions can likely explain the different results observed in our study. For instance, the range of wind speed in the MIZ in our study does not exceed 11 m/s while in their study the wind speed in the marginal ice zone region was within the 10–20 m/s range for several days. This can result in more turbulent sea surface conditions which may have enhanced the sea spray production due to the sea water splashing as a result from the sea-ice interactions.

The regional differences observed for median $N_{0.7c}$ values are not fully consistent with wind speed and wave data. For instance, similarities between median values of open ocean and land $N_{0.7c}$ somewhat contradict the significant difference between the wave properties in these two regions. Additionally, while the median wind speed for the MIZ is slightly larger than the land region, the median $N_{0.7c}$ in the MIZ is ~40% smaller than in the land region. The results hence suggest that the links between the SSA production and wind and wave properties cannot be soley demonstrated through the regional assessment because of atmospheric dispersion, and alternative methods are needed for such assessments as discussed in the next section.

3.3. Collocated variability of aerosol, wind and wave measurements

To better understand possible relations between SSA production, meteorology, and sea surface properties we investigated the relation between collocated $N_{0.7c}$, wave properties, and meteorological data. Since the observed aerosol number concentration relies on both the direct SSA generation mechanisms and factors that influence the transport and loss of SSA in the atmosphere, we take into account atmospheric stability. Atmospheric stability in the MBL can heavily influence the mixing and dispersion of aerosol particles, directly impacting $N_{0.7c}$ (Tedeschi and Piazzola, 2011). Thus, to investigate the impact of the MBL stability on the relationships between wind-wave properties and $N_{0.7c}$ we divided the sample into two subsets corresponding to a stable ($\Delta T_{\text{atm-SST}} > 0$) and an unstable ($\Delta T_{\text{atm-SST}} < 0$) MBL.

As shown in Fig. 6a weak to clear positive covariance exists between wind-wave properties and $N_{0.7c}$ with large scatter in the data for some of the assessed properties. Compared to the total available data, the wind and wave properties for the unstable MLB subset demonstrate a systematically larger covariance to $N_{0.7c}$, with moderate correlation (all $r_{\text{pearson}} > 0.48$) and with statistical significance ($p < 0.05$). H_0 exhibits the strongest correlation to $N_{0.7c}$ ($r_{\text{pearson}} = 0.71$), followed by ε ($r_{\text{pearson}} = 0.55$) and U_{10N} ($r_{\text{pearson}} = 0.49$). The weakest covariance is observed with the inverse wave age. This is expected, because at inverse wave ages <1, the sea state is characterized by swell, which does not induce wave breaking, whereas inverse wave age >1 reflects a wind-driven sea-surface, where waves tend to break. Hence, we expect low $N_{0.7c}$ below 1 and large variability >1. On the other hand, in stable MBL conditions, large scatter was observed between wind-wave properties and $N_{0.7c}$, with an overall weak correlation (all $r_{\text{pearson}} \leq 0.3$ and $p > 0.05$).

Based on the results we hypothesize that MBL mixing state can explain the enhancement of the correlation between sea surface-wind properties and $N_{0.7c}$. An unstable MBL promotes vertical mixing and facilitates the transport and dispersion of the freshly emitted SSA. Therefore, the observed, coarse aerosols under unstable conditions are more likely to represent freshly emitted SSA particles that are instantaneously impacted by wind speed and sea surface state conditions, explaining their higher sensitivity to the sea state and wind speed data. Under stable MBL conditions, vertical mixing is partly inhibited which often results in longer residence time of aerosols in the atmospheric layer above the sea surface. Therefore, we hypothesize that due to the longer aerosol residence time, the stable MBL consists of a mixture of freshly emitted and pre-existing aerosols, which can reduce the covariance between physical properties that promote fresh emission of SSA and the observed aerosol number concentration.

The data suggest that, in addition to wind speed and sea surface properties, the MBL stability can potentially impact the variability of the SSA number concentration. However, the limitation in the number of available data points in our study prevents us from drawing a definitive conclusion regrading such effect. Future studies with larger sample statistics are required to more clearly assess the relation between MBL stability and the major drivers of SSA production.

3.4. Estimation of coarse marine aerosol number concentration from wind-wave properties

Reliance on singular atmospheric or wave parameters is often insufficient for explaining the variability of SSA, due to the underlying complexity of the process which relies both on atmospheric and sea surface state variables (as well as the sea surface micro layer composition (Quinn et al., 2015), which is however beyond the scope of this work). To assess the effectiveness of different physical variables in resolving the coarse aerosol $N_{0.7c}$, we assess how well a set of physically-relevant dimensionless predictors can explain the variability

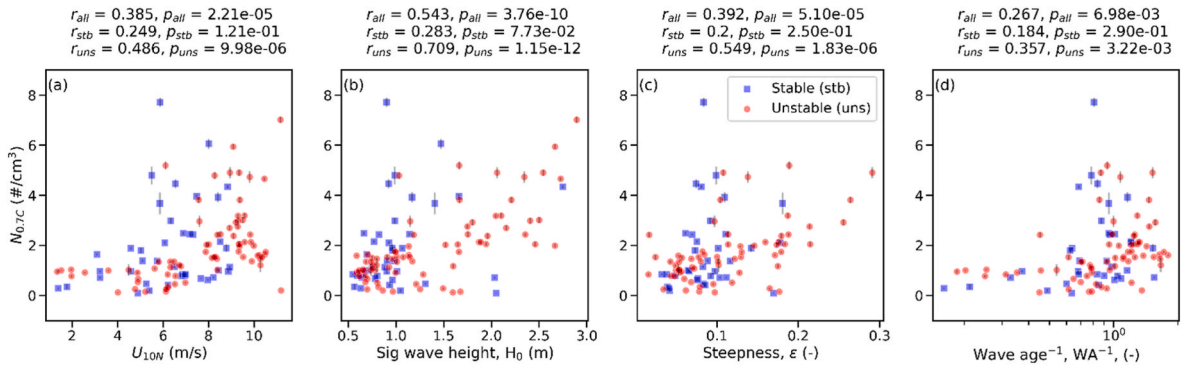

Fig. 6. Scatter plots of collocated measurements of U_{10N} (a), H_0 (b), ε (c), inverse of wave age (d) versus the $N_{0.7c}$ for a stable MBL (blue) and an unstable MBL (red) conditions.

of $N_{0.7c}$ similar to previous studies (Bruch et al., 2021; Lenain and Melville, 2017). For instance, ε can be considered as relevant scaling factor as it is tightly linked to the wave breaking process which generates SSA. Due to the limited range of variability for *SST* (−1.8 to 4.6 °C) and T_{atm} (−3.5 to 4.2 °C) we assumed the water-air density fraction and sea water fluid properties to be constant. Therefore, we avoid including them in the scaling assessment. Thus, the main scaling factors that we consider in our analysis are Re_H, ε, U_{10N}/c. Moreover, to assess the combined effect of these factors, similar to the methodology of Bruch et al. (2021) and Lenain and Melville (2017), we define the product of all the singular factors as a new scaling factor (i.e., $Re_H \times \varepsilon \times U_{10N}/c$). Subsequently, we fit the identified predictors to $N_{0.7c}$ through a power-law relation and use the coefficient of determination (R^2) as a metric to evaluate the effectiveness of given scaling factors to describe $N_{0.7c}$.

Table 1 summarizes the fit results for different tested scaling factors under the stable and unstable boundary layer conditions. The R^2 values for the fits are systematically larger for the unstable MBL condition which is not surprising considering the larger spread and poorer statistics of samples within stable MBL conditions (Fig. 6). For the unstable condition, based on the R^2 values, Re_H provides the best fit to $N_{0.7c}$ data. Fig. 7a and b, show $N_{0.7c}$ versus Re_H along with the fit for the stable and unstable MLB conditions, respectively. The correlation coefficient between Re_H and $N_{0.7c}$ ($r_{pearson} = 0.76$, $R^2 = 0.57$, Fig. 7b) is noticeably larger than between $N_{0.7c}$ with U_{10N} or H_0 alone (Fig. 6). This indicates that $N_{0.7c}$ is much more sensitive to Re_H compared to U_{10N}, which further highlights the importance of combining wave and wind properties for deriving SSA parametrizations. Note, when removing the one data point with high Re_H in Fig. 7a, the relationship becomes even more difficult to describe, which underlines the key finding that in stable boundary layer conditions none of the single or combined variables can successfully describe $N_{0.7c}$ concentrations, most likely because atmospheric residence time and advection play an important role.

The results from the scaling analysis are consistent with a number of studies that have used Re_H as a main variable in parametrizations of SSA flux (Norris et al., 2013; Ovadnevaite et al., 2014; Zhao and Toba, 2001). Furthermore, Brumer et al. (2017) showed that parametrization of whitecap concentration (a major contributing factor to SSA production) with only Re_H as the predictor can be generalized to be the best predictor across different datasets as opposed to more complex wind-wave predictors. Similarly, we observed that combining Re_H with other wave properties (ε and U_{10N}/c) did not enhance the quality of the fit (Table 1). Our results are somewhat in contrast to the findings from other studies that suggested better predictors based on the combination of the Reynold number, wave steepness, and wave age (e.g., Bruch et al., 2021; Lenain and Melville, 2017). It should be noted those two studies were in mid-latitudes and characterised by a rather different range of environmental parameters, such as *SST* and U_{10N}, which might explain the differences.

4. Conclusion

We investigated the relationships between sea state, wind speed, marine boundary layer stability and the occurrence of primary marine aerosol over the Barents and Kara Sea sectors of the Arctic Ocean in the boreal summer of 2021, during the Arctic Century Expedition. We conducted collocated shipborne atmospheric aerosol measurements and sea surface stereo imaging. Sea surface state properties were extracted by processing the stereo images using a state-of-the-art image processing software. We further complemented our dataset with reanalysis data, e.g., sea surface temperature from ERA5.

On the basis of the aerosol count median diameter (CMD) we found two clusters, fine (CMD<0.99 μm) and coarse mode (CMD≥0.99 μm) aerosols (Fig. 3). The coarse aerosol subset has a high correlation with the aerosol mass concentration of Na + Mg ($r_p = 0.90$) indicating a likely association with sea spray aerosol particles. Our analysis showed that the range of variability in wind speed, wave height and steepness, and aerosol number concentration was systematically higher in the open ocean regions as opposed to the marginal ice zone or within 50 km of land (Fig. 4). Calmer sea surface state observed near and in the MIZ are attributed to a dampening effect by the floating ice which impedes the development and subsequent breaking of waves.

Based on all data, correlation analysis indicates weak to moderate positive correlations (r_p = 0.30–0.54) between coarse aerosol number concentration with wind speed, wave height, steepness and wave age. However, by using the difference of the sea surface and atmospheric

Table 1
List of predictors used in the scaling analysis and predictors' fit to $N_{0.7}$ for stable and unstable MBL.

Predictor	Power-law fits (stable MBL condition)	Power-law fits (unstable MBL condition)
ε	$N_{0.7} = 5.6(\varepsilon)^{0.45}\,(R^2 = 0.05)$	$N_{0.7} = 8.1(\varepsilon)^{0.71}\,(R^2 = 0.28)$
$\frac{U_{10N}}{c}$	$N_{0.7} = 2.02\left(\frac{U_{10N}}{c}\right)^{0.42}\,(R^2 = 0.05)$	$N_{0.7} = 1.73\left(\frac{U_{10N}}{c}\right)^{0.56}\,(R^2 = 0.13)$
Re_H	$N_{0.7} = 1.28 \times 10^{-4} Re_H{}^{0.64}\,(R^2 = 0.19)$	$N_{0.7} = 2.90 \times 10^{-6} Re_H{}^{0.86}\,(R^2 = 0.57)$
$\varepsilon \frac{U_{10N}}{c} Re_H$	$N_{0.7} = 6.7 \times 10^{-2}\left(\varepsilon \frac{U_{10N}}{c} Re_H\right)^{0.27}\,(R^2 = 0.1)$	$N_{0.7} = 2.4 \times 10^{-2}\left(\varepsilon \frac{U_{10N}}{c} Re_H\right)^{0.32}\,(R^2 = 0.39)$

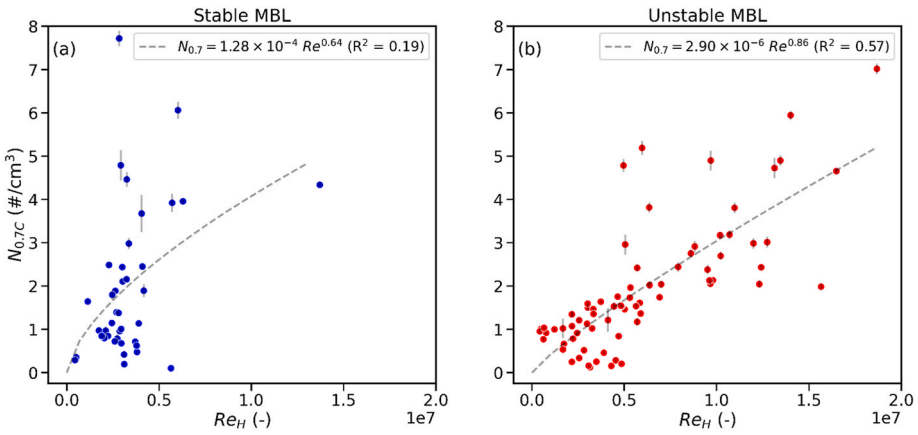

Fig. 7. $N_{0.7c}$ vs Re_H along with the power-law fit for the stable (a) and unstable (b) MBL conditions. While the fit appears to be influenced by a singular point with Re_H of $\sim 1.4 \times 10^7$ in (a), removing this point will result in the reduction of R^2 value to 0.16, which indicates that under stable condition the link between Re_H and $N_{0.7c}$ is weak regardless of this outlier point.

temperature ($\Delta T_{\text{atm-SST}}$) as an indicator of marine boundary layer stability, we show that aerosol number concentration has a systematically higher correlation ($r_p = 0.35$–0.71) to wind and wave properties under unstable MBL conditions ($\Delta T_{\text{atm-SST}} < 0$). The correlation results suggest that during unstable conditions the sensitivity of aerosol particles to the local and instantaneous aerosol generation and dispersion mechanisms (i.e., wind and wave properties) is higher due to the higher mixing capacity of the MBL.

To assess the combined effect of wind and wave properties on aerosol generation we conducted a scaling analysis in which different combinations of dimensionless wind and wave properties were used as predictors for coarse aerosol number concentration. Our results showed that under unstable conditions the wave-height-based Reynold number (Re_H) was the predictor for which the parametrization demonstrated the largest coefficient of determination ($R^2 = 0.57$). Association of SSA generation to Re_H has been reported in previous studies on SSA and sea surface state. The study by Lenain and Melville (2017) indicated that a predictor consisting of the combined Re_H, wave steepness, and wave age ($\varepsilon \frac{U_{10N}}{c} ReH$) is preferable for aerosol concentration parametrizations. However, in our analysis the model based on the $\varepsilon \frac{U_{10N}}{c} ReH$ predictor underperformed compared to only Re_H. This inconsistency could be attributed to the difference in the range of values for wave and wind properties in the summer Arctic, which was much smaller, compared to Lenain and Melville (2017), and our relatively low data availability.

Overall, our results provide insights into the variability of pertinent drivers of SSA production over the Arctic Ocean and demonstrate that a combined consideration of wave properties and wind speed on local SSA generation under certain meteorological conditions is necessary. We further show that specifically for the Arctic Ocean, with lower wind speeds than the Southern Ocean, the marginal sea ice zone is expected to feature smaller SSA concentrations due to the wave dampening effect of the sea ice. Given that the Arctic MIZ increases in extent at the expense of pack ice (Strong and Rigor, 2013), it is important for atmospheric chemistry models to include relevant sea ice and sea state data in their simulations.

Our analysis further shows the applicability of shipborne stereo imaging systems in SSA related research. Based on our results, we conclude that deployment of stereo cameras for acquisition of sea state properties is an important contribution to the study of SSA, since SSA concentrations can be better characterized by considering collocated sea state information. It should be noted that due to statistical limitations of the data and lack of measurements to resolve eddy-covariance information, we were not able to further assess SSA flux parametrizations. Therefore, our results provide a general insight on possible physical variables (sea state, wind and atmospheric stability) that influence SSA production in the Barents and Kara Sea regions over the summer period. Future studies using similar systems could both improve the statistics of collocated atmospheric and wave measurements and integrate flux related variables which in turn can result in the development of more robust SSA parametrizations, specifically for polar regions, which can be integrated into climate models to better represent their role in Arctic amplification.

Code and data availability

The data from this study is available in the open access repository zenodo: https://doi.org/10.5281/zenodo.13372113. The data processing codes are available upon request from AM. The ERA5 reanalysis data by ECMWF is available at https://doi.org/110.24381/cds.adbb2d47 (Hersbach et al., 2023). The AMSR-2 sea ice dataset is produced by European Organisation for the Exploitation of Meteorological Satellites (EUMETSAT) Ocean and Sea Ice Satellite Application Facility (OSI SAF) is available at https://doi.org/10.24381/cds.3cd8b812 (Copernicus Climate Change Service (C3S), 2020).

CRediT authorship contribution statement

Alireza Moallemi: Writing – original draft, Validation, Investigation, Formal analysis, Data curation, Conceptualization. **Alberto Alberello:** Writing – review & editing, Supervision, Investigation. **Iris Thurnherr:** Writing – review & editing, Investigation, Data curation. **Guangyu Li:** Writing – review & editing, Investigation, Data curation. **Zamin A. Kanji:** Writing – review & editing, Supervision, Resources, Funding acquisition. **Filippo Bergamasco:** Writing – review & editing, Supervision, Data curation. **Roman Pohorsky:** Writing – review & editing, Investigation. **Filippo Nelli:** Writing – review & editing, Investigation. **Alessandro Toffoli:** Writing – review & editing, Supervision, Resources. **Julia Schmale:** Writing – review & editing, Supervision, Project administration, Funding acquisition, Conceptualization.

Declaration of competing interest

The authors declare that they have no known competing financial interests or personal relationships that could have appeared to influence the work reported in this paper.

Data availability

The data from this study is available in the open access repository zenodo: https://doi.org/10.5281/zenodo.13372113.

Acknowledgements

This work was funded by the EPFL Center for Imaging [3D Earth-Navigation, 2022]. This research used samples and data provided by the Arctic Century Expedition, a joint initiative led by the Swiss Polar Institute (SPI), the Antarctic and Arctic Research Institute (AARI) and Helmholtz Centre for Ocean Research Kiel (GEOMAR) and funded by the Swiss Polar Foundation. JS holds the Ingvar Kamprad Chair for Extreme Environments Research sponsored by Ferring Pharmaceuticals. AA acknowledges support from EPSRC [EP/Y02012X/1]. ERA5 and reanalysis and sea ice concentration were obtained using Copernicus Climate Change Service Information. The authors thank Alexandre Alahi for his insightful comments on image processing.

Appendix A. Supplementary data

Supplementary data to this article can be found online at https://doi.org/10.1016/j.atmosenv.2024.120844.

References

Alberello, A., Bennetts, L.G., Onorato, M., Vichi, M., MacHutchon, K., Eayrs, C., Ntamba, B.N., Benetazzo, A., Bergamasco, F., Nelli, F., Pattani, R., Clarke, H., Tersigni, I., Toffoli, A., 2022. Three-dimensional imaging of waves and floes in the marginal ice zone during a cyclone. Nat. Commun. 13, 4590. https://doi.org/10.1038/s41467-022-32036-2.

Alkama, R., Taylor, P.C., Garcia-San Martin, L., Douville, H., Duveiller, G., Forzieri, G., Swingedouw, D., Cescatti, A., 2020. Clouds damp the radiative impacts of polar sea ice loss. Cryosphere 14, 2673–2686. https://doi.org/10.5194/tc-14-2673-2020.

Andreae, M.O., Rosenfeld, D., 2008. Aerosol–cloud–precipitation interactions. Part 1. The nature and sources of cloud-active aerosols. Earth Sci. Rev. 89, 13–41. https://doi.org/10.1016/j.earscirev.2008.03.001.

Andreas, E.L., 1992. Sea spray and the turbulent air-sea heat fluxes. J. Geophys. Res.: Oceans 97, 11429–11441. https://doi.org/10.1029/92JC00876.

Ardhuin, F., Stopa, J.E., Chapron, B., Collard, F., Husson, R., Jensen, R.E., Johannessen, J., Mouche, A., Passaro, M., Quartly, G.D., Swail, V., Young, I., 2019. Observing Sea states. Front. Mar. Sci. 6.

Beck, I., Angot, H., Baccarini, A., Dada, L., Quéléver, L., Jokinen, T., Laurila, T., Lampimäki, M., Bukowiecki, N., Boyer, M., 2022. Automated identification of local contamination in remote atmospheric composition time series. Atmos. Meas. Tech. 15, 4195–4224.

Benetazzo, A., 2006. Measurements of short water waves using stereo matched image sequences. Coast. Eng. 53, 1013–1032. https://doi.org/10.1016/j.coastaleng.2006.06.012.

Benetazzo, A., Barbariol, F., Bergamasco, F., Torsello, A., Carniel, S., Sclavo, M., 2015. Observation of Extreme sea waves in a space–time ensemble. J. Phys. Oceanogr. 45, 2261–2275. https://doi.org/10.1175/JPO-D-15-0017.1.

Bergamasco, F., Torsello, A., Sclavo, M., Barbariol, F., Benetazzo, A., 2017. WASS: an open-source pipeline for 3D stereo reconstruction of ocean waves. Comput. Geosci. 107, 28–36. https://doi.org/10.1016/j.cageo.2017.07.001.

Bruch, W., Piazzola, J., Branger, H., van Eijk, A.M.J., Luneau, C., Bourras, D., Tedeschi, G., 2021. Sea-Spray-Generation dependence on wind and wave combinations: a laboratory study. Boundary-Layer Meteorol. 180, 477–505. https://doi.org/10.1007/s10546-021-00636-y.

Brumer, S.E., Zappa, C.J., Brooks, I.M., Tamura, H., Brown, S.M., Blomquist, B.W., Fairall, C.W., Cifuentes-Lorenzen, A., 2017. Whitecap coverage dependence on wind and wave statistics as observed during SO GasEx and HiWinGS. J. Phys. Oceanogr. 47, 2211–2235. https://doi.org/10.1175/JPO-D-17-0005.1.

Cabral, I.S., Young, I.R., Toffoli, A., 2022. Long-term and seasonal variability of wind and wave extremes in the Arctic Ocean. Front. Mar. Sci. 9.

Claeys, M., Roberts, G., Mallet, M., Arndt, J., Sellegri, K., Sciare, J., Wenger, J., Sauvage, B., 2017. Optical, physical and chemical properties of aerosols transported to a coastal site in the western Mediterranean: a focus on primary marine aerosols. Atmos. Chem. Phys. 17, 7891–7915. https://doi.org/10.5194/acp-17-7891-2017.

Dankert, H., Horstmann, J., Lehner, S., Rosenthal, W., 2003. Detection of wave groups in SAR images and radar image sequences. IEEE Trans. Geosci. Rem. Sens. 41, 1437–1446. https://doi.org/10.1109/TGRS.2003.811815.

de Leeuw, G., Andreas, E.L., Anguelova, M.D., Fairall, C.W., Lewis, E.R., O'Dowd, C., Schulz, M., Schwartz, S.E., 2011. Production flux of sea spray aerosol. Rev. Geophys. 49. https://doi.org/10.1029/2010RG000349.

Demoisson, A., Tedeschi, G., Piazzola, J., 2013. A model for the atmospheric transport of sea-salt particles in coastal areas. Atmos. Res. 132–133, 144–153. https://doi.org/10.1016/j.atmosres.2013.04.002.

DeMott, P.J., Hill, T.C.J., McCluskey, C.S., Prather, K.A., Collins, D.B., Sullivan, R.C., Ruppel, M.J., Mason, R.H., Irish, V.E., Lee, T., Hwang, C.Y., Rhee, T.S., Snider, J.R., McMeeking, G.R., Dhaniyala, S., Lewis, E.R., Wentzell, J.J.B., Abbatt, J., Lee, C., Sultana, C.M., Ault, A.P., Axson, J.L., Diaz Martinez, M., Venero, I., Santos-Figueroa, G., Stokes, M.D., Deane, G.B., Mayol-Bracero, O.L., Grassian, V.H., Bertram, T.H., Bertram, A.K., Moffett, B.F., Franc, G.D., 2016. Sea spray aerosol as a unique source of ice nucleating particles. Proc. Natl. Acad. Sci. U.S.A. 113, 5797–5803. https://doi.org/10.1073/pnas.1514034112.

Derkani, M.H., Alberello, A., Nelli, F., Bennetts, L.G., Hessner, K.G., MacHutchon, K., Reichert, K., Aouf, L., Khan, S., Toffoli, A., 2021. Wind, waves, and surface currents in the Southern Ocean: observations from the antarctic circumnavigation expedition. Earth Syst. Sci. Data 13, 1189–1209. https://doi.org/10.5194/essd-13-1189-2021.

Duan, C., Dong, S., Wang, Z., 2019. Wave climate analysis in the ice-free waters of Kara Sea. Regional Studies in Marine Science 30, 100719. https://doi.org/10.1016/j.rsma.2019.100719.

Fitzgerald, J.W., 1991. Marine aerosols: a review. Atmospheric Environment. Part A. General Topics 25, 533–545. https://doi.org/10.1016/0960-1686(91)90050-H.

Gilli, R.S., Karlen, C., Weber, M., Rüegg, J., Barmettler, K., Biester, H., Boivin, P., Kretzschmar, R., 2018. Speciation and mobility of mercury in soils contaminated by legacy emissions from a chemical factory in the rhône valley in canton of valais, Switzerland. Soil Systems 2, 44. https://doi.org/10.3390/soilsystems2030044.

Hersbach, H., Bell, B., Berrisford, P., Biavati, G., Horányi, A., Muñoz Sabater, J., Nicolas, J., Peubey, C., Radu, R., Rozum, I., Schepers, D., Simmons, A., Soci, C., Dee, D., Thépaut, J.-N., 2023. ERA5 hourly data on single levels from 1940 to present. Copernicus Climate Change Service (C3S) Climate Data Store (CDS). https://doi.org/10.24381/cds.adbb2d47.

Hess, M., Koepke, P., Schult, I., 1998. Optical properties of aerosols and clouds: the software package OPAC. Bull. Am. Meteorol. Soc. 79, 831–844. https://doi.org/10.1175/1520-0477(1998)079<0831:OPOAAC>2.0.CO;2.

Hiranuma, N., Brooks, S.D., Moffet, R.C., Glen, A., Laskin, A., Gilles, M.K., Liu, P., Macdonald, A.M., Strapp, J.W., McFarquhar, G.M., 2013. Chemical characterization of individual particles and residuals of cloud droplets and ice crystals collected on board research aircraft in the ISDAC 2008 study. J. Geophys. Res. Atmos. 118, 6564–6579. https://doi.org/10.1002/jgrd.50484.

Hristov, T.S., Miller, S.D., Friehe, C.A., 2003. Dynamical coupling of wind and ocean waves through wave-induced air flow. Nature 422, 55–58. https://doi.org/10.1038/nature01382.

Irish, J.L., Wozencraft, J.M., Cunningham, A.G., Giroud, C., 2006. Nonintrusive measurement of ocean waves: lidar wave gauge. J. Atmos. Ocean. Technol. 23, 1559–1572.

Jiang, B., Xie, Z., Lam, P.K.S., He, P., Yue, F., Wang, L., Huang, Y., Kang, H., Yu, X., Wu, X., 2021. Spatial and temporal distribution of sea salt aerosol mass concentrations in the marine boundary layer from the arctic to the antarctic. J. Geophys. Res. Atmos. 126, e2020JD033892. https://doi.org/10.1029/2020JD033892.

Lafon, C., Piazzola, J., Forget, P., Despiau, S., 2007. Whitecap coverage in coastal environment for steady and unsteady wave field conditions. Journal of Marine Systems, 5th International Symposium on Gas Transfer at Water Surfaces 66, 38–46. https://doi.org/10.1016/j.jmarsys.2006.02.013.

Landwehr, S., Thurnherr, I., Cassar, N., Gysel-Beer, M., Schmale, J., 2020. Using global reanalysis data to quantify and correct airflow distortion bias in shipborne wind speed measurements. Atmos. Meas. Tech. 13, 3487–3506. https://doi.org/10.5194/amt-13-3487-2020.

Lapere, R., Thomas, J.L., Marelle, L., Ekman, A.M.L., Frey, M.M., Lund, M.T., Makkonen, R., Ranjithkumar, A., Salter, M.E., Samset, B.H., Schulz, M., Sogacheva, L., Yang, X., Zieger, P., 2023. The representation of sea salt aerosols and their role in polar climate within CMIP6. JGR Atmospheres 128, e2022JD038235. https://doi.org/10.1029/2022JD038235.

Laussac, S., Piazzola, J., Tedeschi, G., Yohia, C., Canepa, E., Rizza, U., Van Eijk, A.M.J., 2018. Development of a fetch dependent sea-spray source function using aerosol concentration measurements in the North-Western Mediterranean. Atmos. Environ. 193, 177–189. https://doi.org/10.1016/j.atmosenv.2018.09.009.

Lenain, L., Melville, W.K., 2017. Evidence of sea-state dependence of aerosol concentration in the marine atmospheric boundary layer. J. Phys. Oceanogr. 47, 69–84. https://doi.org/10.1175/JPO-D-16-0058.1.

Lewis, E.R., Schwartz, S.E., 2004. Sea salt aerosol production fluxes: estimates and critical analysis. In: Sea Salt Aerosol Production: Mechanisms, Methods, Measurements and Models. American Geophysical Union (AGU), pp. 299–344. https://doi.org/10.1002/9781118666050.ch5.

Li, G., Wieder, J., Pasquier, J.T., Henneberger, J., Kanji, Z.A., 2022. Predicting atmospheric background number concentration of ice-nucleating particles in the Arctic. Atmos. Chem. Phys. 22, 14441–14454. https://doi.org/10.5194/acp-22-14441-2022.

Li, G., Wilbourn, E.K., Cheng, Z., Wieder, J., Fagerson, A., Henneberger, J., Motos, G., Traversi, R., Brooks, S.D., Mazzola, M., China, S., Nenes, A., Lohmann, U., Hiranuma, N., Kanji, Z.A., 2023. Physicochemical characterization and source apportionment of Arctic ice-nucleating particles observed in Ny-Ålesund in autumn 2019. Atmos. Chem. Phys. 23, 10489–10516. https://doi.org/10.5194/acp-23-10489-2023.

Lundgren, K., Vogel, B., Vogel, H., Kottmeier, Ch, 2013. Direct radiative effects of sea salt for the Mediterranean region under conditions of low to moderate wind speeds. J. Geophys. Res. Atmos. 118, 1906–1923. https://doi.org/10.1029/2012JD018629.

Malila, M.P., Thomson, J., Breivik, Ø., Benetazzo, A., Scanlon, B., Ward, B., 2022. On the groupiness and intermittency of oceanic whitecaps. JGR Oceans 127. https://doi.org/10.1029/2021JC017938.

Manabe, S., Wetherald, R.T., 1975. The effects of doubling the CO2 concentration on the climate of a general circulation model. J. Atmos. Sci. 32, 3–15. https://doi.org/10.1175/1520-0469(1975)032<0003:TEODTC>2.0.CO;2.

Mason, B.J., 2001. The role of sea-salt particles as cloud condensation nuclei over the remote oceans. Q. J. R. Meteorol. Soc. 127, 2023–2032. https://doi.org/10.1002/qj.49712757609.

Meredith, M., Sommerkorn, M., Cassotta, S., Derksen, C., Ekaykin, A., Hollowed, A., Kofinas, G., Mackintosh, A., Melbourne-Thomas, J., Muelbert, M.M.C., 2019. Polar regions. Chapter 3, Ipcc Special Report on the Ocean and Cryosphere in a Changing Climate.

Middlemas, E.A., Kay, J.E., Medeiros, B.M., Maroon, E.A., 2020. Quantifying the influence of cloud radiative feedbacks on arctic surface warming using cloud locking in an Earth system model. Geophys. Res. Lett. 47, e2020GL089207. https://doi.org/10.1029/2020GL089207.

Moallemi, A., Landwehr, S., Robinson, C., Simó, R., Zamanillo, M., Chen, G., Baccarini, A., Schnaiter, M., Henning, S., Modini, R.L., Gysel-Beer, M., Schmale, J., 2021. Sources, occurrence and characteristics of fluorescent biological aerosol particles measured over the pristine Southern Ocean. J. Geophys. Res. Atmos. 126, e2021JD034811. https://doi.org/10.1029/2021JD034811.

Monahan, E.C., O'Muircheartaigh, I.G., 1986. Whitecaps and the passive remote sensing of the ocean surface. Int. J. Rem. Sens. 7, 627–642.

Monahan, E.C., Spiel, D.E., Davidson, K.L., 1986. A model of marine aerosol generation via whitecaps and wave disruption. In: Monahan, Edward C., Niocaill, G.M. (Eds.), Oceanic Whitecaps: and Their Role in Air-Sea Exchange Processes, Oceanographic Sciences Library. Springer, Netherlands, Dordrecht, pp. 167–174. https://doi.org/10.1007/978-94-009-4668-2_16.

Moschos, V., Schmale, J., Aas, W., Becagli, S., Calzolai, G., Eleftheriadis, K., Moffett, C.E., Schnelle-Kreis, J., Severi, M., Sharma, S., Skov, H., Vestenius, M., Zhang, W., Hakola, H., Hellén, H., Huang, L., Jaffrezo, J.-L., Massling, A., Nøjgaard, J.K., Petäjä, T., Popovicheva, O., Sheesley, R.J., Traversi, R., Yttri, K.E., Prévôt, A.S.H., Baltensperger, U., Haddad, I.E., 2022. Elucidating the present-day chemical composition, seasonality and source regions of climate-relevant aerosols across the Arctic land surface. Environ. Res. Lett. 17, 034032. https://doi.org/10.1088/1748-9326/ac444b.

Mukherjee, P., Reinfelder, J.R., Gao, Y., 2020. Enrichment of calcium in sea spray aerosol in the Arctic summer atmosphere. Mar. Chem. 227, 103898. https://doi.org/10.1016/j.marchem.2020.103898.

Norris, S.J., Brooks, I.M., Moat, B.I., Yelland, M.J., de Leeuw, G., Pascal, R.W., Brooks, B., 2013. Near-surface measurements of sea spray aerosol production over whitecaps in the open ocean. Ocean Sci. 9, 133–145. https://doi.org/10.5194/os-9-133-2013.

Ovadnevaite, J., Manders, A., de Leeuw, G., Ceburnis, D., Monahan, C., Partanen, A.-I., Korhonen, H., O'Dowd, C.D., 2014. A sea spray aerosol flux parameterization encapsulating wave state. Atmos. Chem. Phys. 14, 1837–1852. https://doi.org/10.5194/acp-14-1837-2014.

Quinn, P.K., Collins, D.B., Grassian, V.H., Prather, K.A., Bates, T.S., 2015. Chemistry and related properties of freshly emitted sea spray aerosol. Chem. Rev. 115, 4383–4399. https://doi.org/10.1021/cr500713g.

Rogers, D.P., 1995. Air-sea interaction: connecting the ocean and atmosphere. Rev. Geophys. 33, 1377–1383. https://doi.org/10.1029/95RG00255.

Rolph, R.J., Feltham, D.L., Schröder, D., 2020. Changes of the arctic marginal ice zone during the satellite era. The Cryosphere 14, 1971–1984. https://doi.org/10.5194/tc-14-1971-2020.

Rossi, G.B., Cannata, A., Iengo, A., Migliaccio, M., Nardone, G., Piscopo, V., Zambianchi, E., 2022. Measurement of sea waves. Sensors 22, 78. https://doi.org/10.3390/s22010078.

Sakerin, S.M., Kruglinsky, I.A., Kabanov, D.M., Kalashnikova, D.A., Kravchishina, M.D., Makarov, V.I., Popova, S.A., Pochufarov, A.O., Simonova, G.V., Turchinovich, YuS., Darin, F.A., 2022. Spatiotemporal variations in atmospheric aerosol characteristics over the Kara, Barents, Norwegian, and Greenland seas (2018–2021 expeditions). Atmos Ocean Opt 35, 651–660. https://doi.org/10.1134/S1024856022060203.

Schmale, J., Baccarini, A., Thurnherr, I., Henning, S., Efraim, A., Regayre, L., Bolas, C., Hartmann, M., Welti, A., Lehtipalo, K., Aemisegger, F., Tatzelt, C., Landwehr, S., Modini, R.L., Tummon, F., Johnson, J.S., Harris, N., Schnaiter, M., Toffoli, A., Derkani, M., Bukowiecki, N., Stratmann, F., Dommen, J., Baltensperger, U., Wernli, H., Rosenfeld, D., Gysel-Beer, M., Carslaw, K.S., 2019. Overview of the antarctic circumnavigation expedition: study of preindustrial-like aerosols and their climate effects (ACE-SPACE). Bull. Am. Meteorol. Soc. 100, 2260–2283. https://doi.org/10.1175/BAMS-D-18-0187.1.

Schumacher, A., 1939. Stereophotogrammetrische Wellenaufnahmen. W. de Gruyter.

Schwendeman, M.S., Thomson, J., 2017. Sharp-crested breaking surface waves observed from a ship-based stereo video system. J. Phys. Oceanogr. 47, 775–792. https://doi.org/10.1175/JPO-D-16-0187.1.

Shupe, M.D., Intrieri, J.M., 2004. Cloud radiative forcing of the arctic surface: the influence of cloud properties, surface albedo, and solar zenith angle. J. Clim. 17, 616–628. https://doi.org/10.1175/1520-0442(2004)017<0616:CRFOTA>2.0.CO;2.

Smith, M., Thomson, J., 2020. Pancake sea ice kinematics and dynamics using shipboard stereo video. Ann. Glaciol. 61, 1–11. https://doi.org/10.1017/aog.2019.35.

Song, A., Li, J., Tsona, N.T., Du, L., 2023. Parameterizations for sea spray aerosol production flux. Appl. Geochem. 157, 105776. https://doi.org/10.1016/j.apgeochem.2023.105776.

Song, C., Dall'Osto, M., Lupi, A., Mazzola, M., Traversi, R., Becagli, S., Gilardoni, S., Vratolis, S., Yttri, K.E., Beddows, D.C.S., Schmale, J., Brean, J., Kramawijaya, A.G., Harrison, R.M., Shi, Z., 2021. Differentiation of coarse-mode anthropogenic, marine and dust particles in the High Arctic islands of Svalbard. Atmos. Chem. Phys. 21, 11317–11335. https://doi.org/10.5194/acp-21-11317-2021.

Stopa, J.E., Ardhuin, F., Girard-Ardhuin, F., 2016. Wave climate in the Arctic 1992–2014: seasonality and trends. Cryosphere 10, 1605–1629. https://doi.org/10.5194/tc-10-1605-2016.

Strong, C., Rigor, I.G., 2013. Arctic marginal ice zone trending wider in summer and narrower in winter. Geophys. Res. Lett. 40, 4864–4868. https://doi.org/10.1002/grl.50928.

Struthers, H., Ekman, A.M.L., Glantz, P., Iversen, T., Kirkevåg, A., Seland, Ø., Mårtensson, E.M., Noone, K., Nilsson, E.D., 2013. Climate-induced changes in sea salt aerosol number emissions: 1870 to 2100. J. Geophys. Res. Atmos. 118, 670–682. https://doi.org/10.1002/jgrd.50129.

Tedeschi, G., Piazzola, J., 2011. Development of a 2D marine aerosol transport model: application to the influence of thermal stability in the marine atmospheric boundary layer. Atmos. Res. 101, 469–479. https://doi.org/10.1016/j.atmosres.2011.04.013.

Tersigni, I., Alberello, A., Messori, G., Vichi, M., Onorato, M., Toffoli, A., 2023. High-resolution thermal imaging in the antarctic marginal ice zone: skin temperature heterogeneity and effects on heat fluxes. Earth Space Sci. 10, e2023EA003078. https://doi.org/10.1029/2023EA003078.

Toffoli, A., Alberello, A., Clarke, H., Nelli, F., Benetazzo, A., Bergamasco, F., Ntamba, B. N., Vichi, M., Onorato, M., 2023. Observations of Rogue Seas in the Southern Ocean arXiv preprint arXiv:2310.01841.

Veron, F., 2015. Ocean spray. Annu. Rev. Fluid Mech. 47, 507–538. https://doi.org/10.1146/annurev-fluid-010814-014651.

Waseda, T., Alberello, A., Nose, T., Toyota, T., Kodaira, T., Fujiwara, Y., 2022. Observation of anomalous spectral downshifting of waves in the okhotsk sea marginal ice zone. Phil. Trans. R. Soc. A. 380, 20210256. https://doi.org/10.1098/rsta.2021.0256.

Xu, W., Ovadnevaite, J., Fossum, K.N., Lin, C., Huang, R.-J., Ceburnis, D., O'Dowd, C., 2022. Sea spray as an obscured source for marine cloud nuclei. Nat. Geosci. 15, 282–286. https://doi.org/10.1038/s41561-022-00917-2.

Xu, X., Voermans, J.J., Ma, H., Guan, C., Babanin, A.V., 2021. A wind–wave-dependent sea spray volume flux model based on field experiments. J. Mar. Sci. Eng. 9, 1168. https://doi.org/10.3390/jmse9111168.

Yan, J., Jung, J., Lin, Q., Zhang, M., Xu, S., Zhao, S., 2020. Effect of sea ice retreat on marine aerosol emissions in the Southern Ocean, Antarctica. Sci. Total Environ. 745, 140773. https://doi.org/10.1016/j.scitotenv.2020.140773.

Zhao, D., Toba, Y., 2001. Dependence of whitecap coverage on wind and wind-wave properties. J. Oceanogr. 57, 603–616. https://doi.org/10.1023/A:1021215904955.

Zinke, J., Nilsson, E.D., Zieger, P., Salter, M.E., 2022. The effect of seawater salinity and seawater temperature on sea salt aerosol production. J. Geophys. Res. Atmos. 127, e2021JD036005.